Available online at www.sciencedirect.com
SCIENCE DIRECT®
International Journal of Heat and Mass Transfer 47 (2004) 4459–4468
International Journal of HEAT and MASS TRANSFER
www.elsevier.com/locate/ijhmt

Drying of a porous spherical rock for compressed air energy storage

Abraham Dayan [a], Joseph Flesh [a], Craig Saltiel [b,*]

[a] Department of Fluid Mechanics and Heat Transfer, Tel-Aviv University, Ramat Aviv, Israel
[b] Synergetic Technologies Inc., One University Place, Suite D120, Rensselaer, NY 12144, USA

Received 10 May 2003; received in revised form 1 February 2004

Abstract

A model for compressed hot air storage in a sedimentary porous rock composed of spherical rock is presented. During charging, the rock loses moisture and a dry spherical shell develops around a moist zone. The transient heat conduction, convection and mass transfer that take place during charging and discharging are simulated using a moving-grid numerical methodology for both the wet and dry zones. A process of evaporation/condensation moves the boundary between the two zones. The model is verified using data from a concrete drying experiment. A parametric study is conducted to demonstrate the sensitivity of the system to various parameters.

Keywords: Compressed air energy storage; Porous media; Drying; Heat and mass transfer

1. Introduction

Underground compressed air energy storage (CAES) has been considered as an attractive means of load management in power plants [1] and new cycles combining air humidification, coal gasification and compressed air energy storage have been explored [2]. Economic and performance analysis has shown that CAES plants can substantially enhance the economics of conventional gas turbine power plants. Compressed air energy storage is more efficient and less expensive than conventional hydraulic pumped storage facilities [3]. Recently, the Alabama Electric Co-operative installed a 110 MW CAES plant at McIntosh, Al [4], where both high and low pressure combustors were tested. Compressed air energy storage has attracted increased attention throughout the world (for instance, Germany has an operational plant at Huntorf, and plans are underway to construct a CAES plant in Israel).

While conceptual and pragmatic system studies of compressed air energy storage have been performed, more detailed analysis of air impregnation in natural underground porous aquifers is needed. Exploitation of this technology requires development of adequate computational tools to model aquifers and optimize air storage operations and economics. In particular, heat and mass transfer studies are required to develop air charge/discharge strategies in terms of porous bed characteristics: porosity, permeability, and thermal conductivity of sedimentary rock. Evaluation of characteristic aquifer dimensions, both on macro (the entire available underground region) and micro scales, is necessary to assess the aquifer storage capacity and determine the number and location of wells. Detailed evaluations are needed to determine energy recovery efficiency.

Most aquifers are inhomogeneous—essentially a network of fissured rock. It is customary, however, to consider the fissured rocks as porous homogeneous blocks separated by gaps (representing the fissures) [5]. Thus, the aquifer is a double porosity zone, where blocks and fissures each have their own characteristic

* Corresponding author. Tel.: +1-518-525-2650.
E-mail address: csaltiel@synergetic-tech.com (C. Saltiel).

0017-9310/$ - see front matter © 2004 Elsevier Ltd. All rights reserved.
doi:10.1016/j.ijheatmasstransfer.2004.05.006

Nomenclature

C	constant volume heat capacity
C_p	constant pressure heat capacity
D	species mass diffusion coefficient
$\overline{D}$	dimensionless mass diffusion coefficient of vapor into air $\left(\frac{D}{\varepsilon}\frac{C_0\rho_0}{K_d}\right)$
e	specific energy
$\bar{e}$	dimensionless specific energy $\left(\frac{e}{C_0T_s}\right)$
h	specific enthalpy
$\bar{h}$	dimensionless specific enthalpy $\left(\frac{h}{C_0T_s}\right)$
h^*	convective heat transfer coefficient at the sphere surface
h_{fg}	vaporization specific latent enthalpy
j	mass diffusion flux
$\overline{J}$	dimensionless mass diffusion flux $\left(j\frac{C_0R}{K_d\varepsilon}\right)$
K	thermal conductivity
k	permeability
$\bar{k}$	dimensionless permeability $\left(k\frac{C_0\rho_aP_s}{K_d\varepsilon\mu}\right)$
P	pressure
$\overline{P}$	dimensionless pressure (P/P_s)
q	radial heat flux on the sphere surface
R	sphere radius
r	radius
$\bar{r}$	dimensionless radius (r/R)
S	fraction of pore space occupied by gaseous species
T	absolute temperature
$\overline{T}$	dimensionless temperature (T/T_s)
T_r	energy reference temperature
t	time
$\bar{t}$	dimensionless time $\left(\frac{K_d}{\rho_0C_0R^2}t\right)$
u	velocity
ω	mass fraction
β	gas over liquid viscosity ratio
ε	porosity
μ	viscosity
ρ	specific mass
$\bar{\rho}$	dimensionless specific mass (ρ/ρ_0)
η	dimensionless radial distance from the dry/wet interface into the dry zone, see Eq. (8)
ς	dimensionless radial distance from the dry/wet interface into the wet zone, see Eq. (8)
σ	wet over dry zone thermal conductivity ratio
ξ	radius of the dry/wet interface position divided by R
$\dot{\xi}$	dimensionless time derivative of the dry/wet interface location
Δ	finite difference

Indices

d	dry zone property
g	gaseous species property
i	dummy index or spatial numerical grid index
int	dry/wet interface
j	numerical time step index
l	property of liquid
out	condition around the sphere
s	initial condition
w	wet zone property
0	property of the solid porous matrix material
1	water property
2	vapor property
3	air property
–	dimensionless property

porosity. The volume of the block pores far exceeds the fissure volume. Therefore, air storage would take place primarily within the block pores. In contrast, the permeability of the fissures far surpasses that of the blocks. Therefore, the flow of air between the well and the various blocks of the reservoir would preferentially be through the fissures.

Blocks and fissures can vary in shape, size and geometry. From a statistical viewpoint, and in the perspective of examining the flow and storage of air in the entire aquifer, it is most useful to conceptualize the local blocks as homogeneous porous spheres. The aquifer can be modeled as a domain comprised of many groups of homogeneous spheres of different characteristic dimensions and properties. In addition, each sphere is expected to have different boundary conditions, i.e., the temperature and pressure of the fluid in the fissure surrounding the porous sphere. The local thermal/fluid conditions of each sphere and its surroundings will depend on the sphere location in the aquifer (specifically, its distance from charge/discharge points, or wells).

Individual spherical structures can be classified as homogeneous with respect to their permeability and porosity. Initially, prior to air insertion, the blocks contain both liquid and vapor. Once hot compressed air is forced into the porous sphere, the liquid gradually evaporates and a dry zone develops along the outer surface of the porous rock. The dry zone expands over time due to repeated evaporation in each charging/discharging cycle. Consequently, the boundary between the wet (liquid and vapor) and dry (compressed air and vapor) zones moves towards the sphere center over time as water evaporates. During the charging cycle (penetration of hot air into the block), evaporation takes place exclusively at the dry/wet interface, where the wet zone temperature is the highest. Vapor advec-

ted from the interface into the wet zone partially recondenses to maintain local thermodynamic equilibrium conditions.

The physical aspects of simultaneous heat and mass transfer with phase change in a porous media are described extensively by Kaviany [6], which includes discussion of several studies of moving phase-change fronts. The characteristics of the drying process depend on moisture content, the dry zone temperature relative to moisture saturation temperature, and the stability of the evaporation front interface. Numerous investigations of the two-phase evaporation front regime and its stability [7,8] have been conducted. When bounding a liquid saturated region (funicular flow regime), the evaporation front is often modeled as a two-phase region [9,10]. However, when treating problems of low moisture content, the evaporation front is idealized as just a surface that separates the moist and dry regions [11]. In our model, this simplification is invoked and we assume that the evaporation front is stable.

Characterization of drying modes and drying times of a single sphere is an important first step for the development of a comprehensive model for the entire aquifer. In this work, we approach this task by developing a model to simulate the heat and mass transfer in a typical moist porous sphere as it is constantly or cyclically charged with hot, dry compressed air. A numerical procedure is developed to describe the processes of heat conduction, heat convection, and mass transfer owing to pressure and concentration gradients in the wet and dry zones. Transient variations of temperature, pressure, and water content spatial profiles, and the steam flux exiting the rock surface are explored. While the model developed in this work is targeted for use as a component of a comprehensive design code for compressed air energy storage facilities, it can also be employed for analyzing other drying applications, e.g., clinker formation during the calcining of cement in kilns and food processing and preparation [12]. The problem is also similar to the drying of rocks used for radioactive material deposition [13].

2. Problem description and mathematical model

Fig. 1 shows a schematic diagram of a typical region in a porous aquifer consisting of blocks separated by formation fissures. The blocks have different geometries, orientations and sizes and can be represented as spheres that portray their characteristic dimensions (i.e., both their volumetric storage capacities and transport response time attributes). Furthermore, a spherical shape can be regarded as a reasonable average geometry for different block shapes and orientations. The fissures are merely flow communication channels with negligible storage capacity. Their characteristic dimensions and permeability are determined via in situ tests.

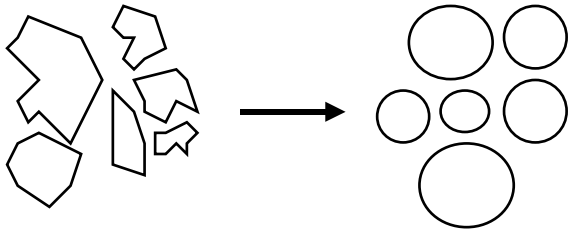

Fig. 1. Schematic depiction of a typical region in a porous aquifer and its model representation.

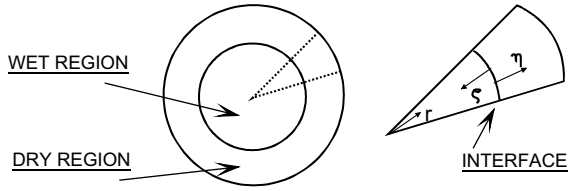

Fig. 2. Physical model of a spherical porous block with a core surrounded by a dry shell.

To study the response of one spherical block to a surge of hot compressed air in the surrounding fissure (penetration of hot air in a charging cycle), two distinct regions in each sphere are modeled; one dry and the other wet (see Fig. 2). This dry/wet modeling approach was successfully employed for studying the drying of a concrete planar wall subject to a step change in its surface temperature [14]. Compressed air, at temperatures well above that of the aquifer fluid, penetrates the sphere, drying it from the outside inwards. The center directed heat flux penetrates both the wet and the dry regions and supports evaporation of water at the interface. The migration of the liquid moisture within the blocks is governed primarily by pressure gradients. Transport of vapor and air, on the other hand, is driven by both pressure and concentration gradients. During the charging phase, vapor generated at the dry/wet interface recondenses within the relatively colder wet region, thus slowing down the drying process of the blocks.

The governing equations of the physical model are based on the following transport laws and thermodynamic equations of state. The gaseous mixture (air and vapor) filtration velocity in the dry zone, according to Darcy's Law, is

$$u_g = -S\frac{k_d}{\mu_g}\nabla P \tag{1}$$

where P denotes the pore pressure, k_d the dry zone permeability, S the pore volumetric fraction occupied by

gas (assuming that the gas effective permeability is proportional to S), and μ_g the gas viscosity. Similarly, the liquid velocity u_l is also determined via Darcy's Law, with an effective permeability of $(1-S)k_d$,

$$u_l = -(1-S)\frac{k_d}{\mu_l}\nabla P \tag{2}$$

The Fourier law was applied to calculate thermal conductivity fluxes with two different coefficients, K_d and K_w for the dry and wet zones, respectively. The mass diffusive flux of the vapor in the dry and wet zones were calculated according to Fick's law

$$j_2 = -\varepsilon \cdot S \cdot D(\rho_2 + \rho_3)\frac{\partial \omega_2}{\partial r} \tag{3}$$

where ω_2 denotes the mass fraction of the vapor, and ρ_2 and ρ_3 are the vapor and air specific mass, respectively, D is the diffusion coefficient of vapor in air, and ε is the porosity. The presence of the liquid has an effect of reducing the available pore space for mass diffusion, in the same manner that pores reduce the space for mass diffusion. Therefore, the effective diffusivity was assumed to be proportional to εS (notice that $S = 1$ in the dry zone).

Since the density, pressure and temperature of the gaseous species are in local thermodynamic equilibrium, the transport equations are coupled with thermodynamic equations of state. Air and water vapor are treated as an ideal binary mixture that obey Dalton's Law

$$\begin{aligned} P_i &= \rho_i R_i^* T \\ e_i &= C_i(T - T_r) \\ h_i &= C_{pi}(T - T_r) \\ P &= (\rho_2 R_2^* + \rho_3 R_3^*)T \end{aligned} \tag{4}$$

where R_i^* is the gas constant of the ith gas species, T is the absolute temperature, T_r the energy reference temperature, and C and C_p are the specific heat at constant volume and pressure, respectively. The water density and specific heats can be assumed constant. The specific enthalpy of water is calculated according to

$$h_l = C_l(T - T_r) - h_{fg} \tag{5}$$

where h_{fg} is the specific heat of vaporization at constant pressure at T_r.

In the wet region, the vapor is saturated owing to the local equilibrium assumption. This is justified in view of the enormous specific pore surface area of the rock structure and its low permeability. Hence, the vapor pressure was calculated according to

$$P_2 = 1.055 \times 10^{21} T^{-5} \exp\left(-\frac{7000}{T}\right) \tag{6}$$

where P is expressed in atmospheres and T in degrees Kelvin.

At the sphere boundary ($r = R$), the pressure and heat flux are functions of the ambient conditions (fracture space), i.e. temperature (T_{out}) and pressure (P_{out})

$$\begin{aligned} &P = P_{out}(t) \\ &q = h^*(T - T_{out}(t)) \quad \text{at } r = R \end{aligned} \tag{7}$$

where h^* is the heat transfer coefficient at the sphere surface. Note that both the pressure and heat flux are transient.

Liquid, vapor, and air transport within the porous sphere must satisfy a set of conservation equations for mass and energy. Because of differences in properties, two sets of conservation equations are written, one for the wet region and one for the dry zone. For ease and generality of presentation, the conservation equations are presented in dimensionless form in spherical coordinates (the dimensionless definitions of the various parameters can be found in the nomenclature). Following Saito and Seki [15], the origin of the dimensionless radial coordinate is positioned at the interface between the wet and dry zones, as shown in Fig. 2. Accordingly, the dimensionless coordinate system is based on the following definitions:

$$\begin{aligned} \bar{r} &= r/R \\ \xi &= r_{int}/R \\ \eta &= \frac{\bar{r}_d - \xi}{1 - \xi} \\ \varsigma &= \frac{\xi - \bar{r}_w}{\xi} \end{aligned} \tag{8}$$

where the subscripts "int" indicates the dry/wet interface position, and 'd' and 'w' the dry and wet regions, respectively. The respective mass continuity equation for the dry zone can be expressed as

$$\begin{aligned} \frac{\partial \bar{\rho}_i}{\partial \bar{t}} = \frac{1}{\bar{r}^2(1-\xi)^2}\frac{\partial}{\partial \eta}\left\{\bar{r}^2\left[\bar{k}\bar{\rho}_i\frac{\partial \overline{P}}{\partial \eta} + \overline{J}_i\right]\right\} \\ + \frac{\partial \bar{\rho}_i}{\partial \eta}\frac{1-\eta}{1-\xi}\dot{\xi} \quad i = 2,3 \end{aligned} \tag{9}$$

where the dimensionless parameters are density $\bar{\rho}$, time $\bar{t}$, permeability $\bar{k}$, pressure $\overline{P}$, and mass diffusion flux $\overline{J}$ (notice that $\overline{J}_2 = -\overline{J}_3$). The indices $i = 1, 2, 3$ represent liquid, vapor and air, respectively. In essence, the equation indicates that the rate of mass accumulation equals the divergence of the filtration and diffusion mass fluxes. The last term on the right-hand side of the equation is a convective term resulting from the incorporation of the moving coordinate system.

The energy conservation equation for the dry zone is

$$\frac{\partial}{\partial \bar{t}}\left[\frac{1-\varepsilon}{\varepsilon}\overline{T}+\sum_{i=2}^{3}(\bar{\rho}_i\bar{e}_i)\right] = \frac{\partial}{\partial \eta}\left[\frac{1-\varepsilon}{\varepsilon}\overline{T}+\sum_{i=2}^{3}(\bar{\rho}_i\bar{e}_i)\right]\frac{1-\eta}{1-\xi}\dot{\xi}+\frac{1}{\bar{r}^2(1-\xi)^2} \times\frac{\partial}{\partial \eta}\left\{\bar{r}^2\left[\frac{1}{\varepsilon}\frac{\partial \overline{T}}{\partial \eta}+\bar{k}\sum_{i=2}^{3}(\bar{\rho}_i\bar{h}_i)\frac{\partial \overline{P}}{\partial \eta}+\sum_{i=2}^{3}(\overline{J_i h_i})\right]\right\} \tag{10}$$

where $\bar{e}$ is the dimensionless specific internal energy, $\overline{T}$ the dimensionless temperature, and $\overline{h}$ the dimensionless specific enthalpy. The left-hand side of the equation represents the rate of energy accumulation in the solid matrix and gaseous constituents. The first term in the right-hand side stems from the adoption of the moving coordinate system, the second term contains the divergence of all three fluxes: heat conduction, heat convection (filtration) and energy transport via mass diffusion.

The respective wet zone vapor mass conservation is

$$\frac{\partial}{\partial \bar{t}}[(1-S)\bar{\rho}_1+S\bar{\rho}_2] = -\frac{\partial}{\partial \varsigma}[(1-S)\bar{\rho}_1+S\bar{\rho}_2]\frac{1-\varsigma}{\xi}\dot{\xi}+\frac{1}{\xi^2(1-\varsigma)^2} \times\frac{\partial}{\partial \varsigma}\left\{(1-\varsigma)^2\left[\bar{k}(\beta(1-S)\bar{\rho}_1+S\bar{\rho}_2)\frac{\partial \overline{P}}{\partial \varsigma}+\overline{J}_2\right]\right\} \tag{11}$$

and the wet zone energy equation is

$$\frac{\partial}{\partial \bar{t}}\left[\frac{1-\varepsilon}{\varepsilon}\overline{T}+(1-S)\bar{\rho}_1\bar{e}_1+S\sum_{i=2}^{3}(\bar{\rho}_i\bar{e}_i)\right] = -\frac{\partial}{\partial \varsigma}\left[\frac{1-\varepsilon}{\varepsilon}\overline{T}+(1-S)\bar{\rho}_1\bar{e}_1+S\sum_{i=2}^{3}(\bar{\rho}_i\bar{e}_i)\right]\frac{1-\varsigma}{\xi}\dot{\xi} +\frac{1}{\xi^2(1-\varsigma)^2}\frac{\partial}{\partial \varsigma}\left\{(1-\varsigma)^2\left[\frac{\sigma}{\varepsilon}\frac{\partial \overline{T}}{\partial \varsigma} +\bar{k}\left[(1-S)\beta\bar{\rho}_1\bar{h}_1+S\sum_{i=2}^{3}(\bar{\rho}_i\bar{h}_i)\right]\frac{\partial \overline{P}}{\partial \zeta}+\sum_{i=2}^{3}(\overline{J}_i\bar{h}_i)\right]\right\} \tag{12}$$

where β is the gas mixture viscosity divided by the water viscosity and σ is the wet to dry zone thermal conductivity ratio. The wet zone equations are similar to the dry zone and they contain an additional parameter (S) that accounts for the presence of two phases in the pore space.

The mass continuity equation for air in the wet zone is

$$\frac{\partial}{\partial \bar{t}}(S\bar{\rho}_3) = -\frac{\partial}{\partial \varsigma}(S\bar{\rho}_3)\frac{1-\varsigma}{\xi}\dot{\xi}+\frac{1}{\xi^2(1-\varsigma)^2} \times\frac{\partial}{\partial \varsigma}\left\{(1-\varsigma)^2\left[\bar{k}S\bar{\rho}_3\frac{\partial \overline{P}}{\partial \varsigma}+\overline{J}_3\right]\right\} \tag{13}$$

At the dry/wet interface three additional requirements are imposed. The first requires that continuity of the air flux must hold across the interface. The second requires that liquid mass lost at the interface must equal to the sum of the vapor fluxes entering both the dry and wet zones in addition to the liquid flux entering the wet zone. Likewise, the energy conducted to the interface must equal the sum of the energy conducted into the wet zone, the latent heat consumed for liquid vaporization, and all the species enthalpies (liquid, vapor and air) transported from the interface.

The initial and boundary conditions vary according to the specific problem of interest. All solutions must, however, satisfy the symmetry condition at the sphere center $\zeta = 1$ $(r = 0)$ for temperature, pressure, pore volume fraction and density

$$\frac{\partial \overline{P}}{\partial \varsigma}=\frac{\partial \overline{T}}{\partial \varsigma}=\frac{\partial S}{\partial \varsigma}=\frac{\partial \bar{\rho}_i}{\partial \varsigma}=0 \quad \text{at } r=0 \tag{14}$$

3. Solution method

Fig. 3 contains a flow chart depicting the procedure used to numerically determine the dimensionless pressure, temperature, density, and the fraction of the pore space occupied by the gaseous species (S). An explicit moving-grid, finite difference numerical solution is employed to solve the governing nonlinear conservation equations for any arbitrary initial and boundary condition. The wet and dry regions of the sphere are discretized with equally spaced nodes (25 nodes on each side of the dry/wet interface).

The stability of the numerical calculations is assured via six criteria for maximum permissible time increments. These criteria can be developed via a Taylor series approximation for heat and mass transport in the dry and wet regions (including at their boundaries) [16]. Denoting i as a spatial nodal point and j as a temporal nodal point, the stability criteria can be expressed as

(1) filtration and mass diffusion in the dry zone

$$\Delta \bar{t} \leqslant \frac{1}{2[\overline{P}(i,j)\bar{k}+\overline{D}]}\left[\frac{\bar{r}_d(i,j)}{\bar{r}_d(i+1/2,j)}\right]^2[\Delta\eta\cdot(1-\xi(j))]^2 \tag{15}$$

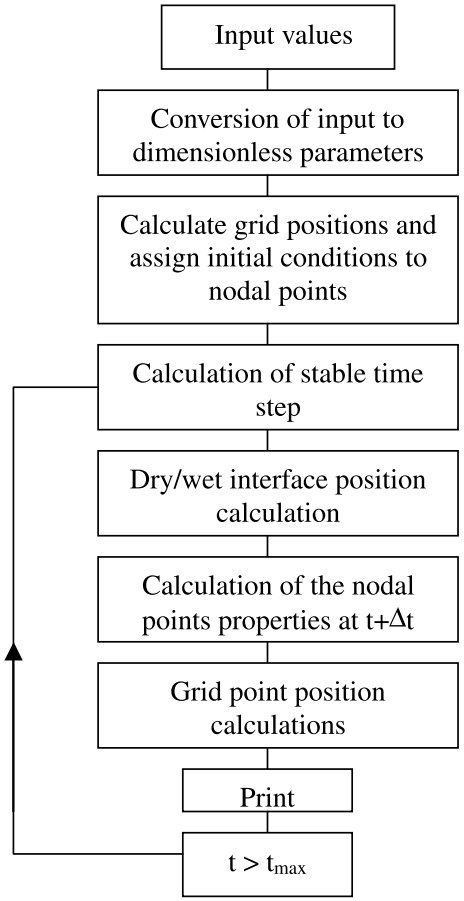

Fig. 3. Flow chart depicting numerical scheme.

(2) filtration and mass diffusion in the wet zone

$$\Delta\bar{t} \leqslant \frac{1}{2[\overline{P}(i,j)\bar{k}+\overline{D}]}\left[\frac{1-\varsigma(i)}{1-\varsigma(i-1/2)}\right]^2[\Delta\varsigma\cdot\xi(j)]^2 \tag{16}$$

(3) heat conduction in the dry zone, evaluated at the first grid in the dry zone $i = 1$ (closest to the sphere center)

$$\Delta\bar{t} \leqslant \frac{1}{2\varepsilon}\left[\frac{\bar{r}_d(i,j)}{\bar{r}_d(i+1/2,j)}\right]^2[\Delta\eta\cdot(1-\xi(j))]^2 \quad \text{at } i=1 \tag{17}$$

(4) heat conduction in the wet zone, evaluated at the last grid in the wet zone $i = n_w$ (closest to the sphere center)

$$\Delta\bar{t} \leqslant \frac{\sigma}{2\varepsilon}\left[\frac{1-\varsigma(i)}{1-\varsigma(i-1/2)}\right]^2[\Delta\varsigma\cdot\xi(j)]^2 \quad \text{at } i=n_w \tag{18}$$

(5) heat conduction at the boundary $r = R$, where n_b is the index of the grid near the sphere surface

$$\Delta\bar{t} \leqslant \frac{1}{4\varepsilon}[\bar{r}(i,j)]^2[\Delta\eta\cdot(1-\xi(j))]^2 \quad \text{at } i=n_b \tag{19}$$

(6) filtration and mass diffusion at the boundary $r = R$

$$\Delta\bar{t} \leqslant \frac{1}{[4\overline{P}(i,j)\bar{k}+\overline{D}]}[\bar{r}_d(i,j)]^2[\Delta\eta \cdot(1-\xi(j))]^2 \quad \text{at } i=n_b. \tag{20}$$

The time step chosen to conduct each numerical calculation is the smallest of the above criteria.

As a validation test for the code, simulation results were compared with experimental data on dehydration [17] of a concrete cylindrical slab. The numerical code was generalized to model drying in either Cartesian, cylindrical or polar coordinate systems [18]. In the experiment, a 0.6 m diameter slab of thickness 0.3 m was heated by a steel plate on one side and maintained at room temperature on the other side. Temperatures and pressures were measured along several axial locations and vapor released from the concrete was collected and weighed throughout the experiment. Details of test conditions can be found in [12] and [17], material properties are taken from [19].

Figs. 4 and 5 depict the variation of temperature and total vapor discharged from the heated surface per unit area over time. Excellent agreement is found between the experiment and simulation results, providing confidence in the numerical approach. Fig. 4 shows the temperature rising with time at different locations in the slab. The linear slope in Fig. 5, after an initial transition period, shows that the rate of vapor discharge remains fairly constant over time.

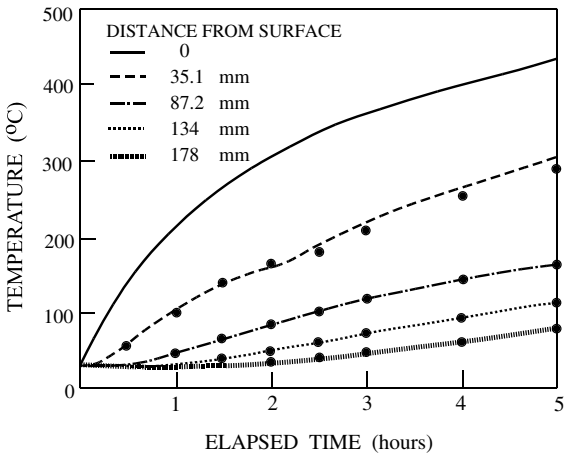

Fig. 4. Calculated and measured temperature response at various depths from the heated surface.

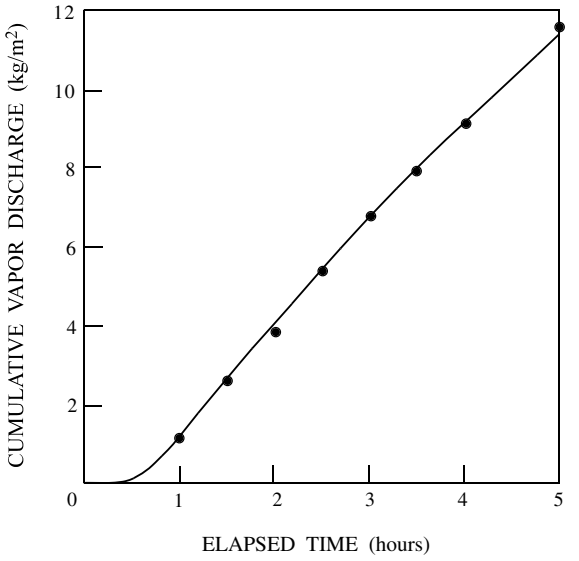

Fig. 5. Calculated and measured cumulative vapor mass released, from the heated surface, per unit surface area over time.

4. Results and discussion

We simulate the charging of an aquifer with compressed hot air by calculating the transient temperature, pressure, and moisture distributions in a porous sphere composed of dolomite stone (whose properties can be found in Table 1). The initial thermodynamic conditions of the porous sphere are listed in Table 2. At time $\bar{t} = 0$, the outer wall of the sphere is suddenly exposed to a step change in temperature ($T_{out} = 250$ °C) and pressure ($P_{out} = 45$ atm). A heat flux, $q = h(T_{out} - T_{wall})$, is thus imposed at the wall and pressurized hot air is driven into the sphere by the large pressure gradient. Vapor consequently migrates outwards and is released from the sphere surface into the fissure space. Periodic or continuous exposure to high temperature compressed air would eventually dry out the spherical rock completely.

Table 1
Input data on material properties and operating conditions for the results shown in Figs. 6–10, taken from [19]

P_s	40×10^5 Pa
T_s	21 °C
S_s	0.7
k/μ_g	5×10^{-13} m²/(Pa s)
k/μ_l	0.0 m²/(Pa s)
D	5×10^{-7} m²/s
h^*	50 W/(m² °C)
ε	0.05
ρ_0	2500.0 kg/m³
C_2	1000.0 J/(kg °C)
K_d	2.5 W/(m °C)
K_w	2.5 W/(m °C)
T_{out}	250.0 °C
P_{out}	45×10^5 Pa

Table 2
The corresponding dimensionless parameters of Table 1

$\bar{k}$	40.0
β	0.0
$\overline{D}$	10.0
σ	1.0
S_s	0.7
$\overline{T}_{out}$	1.604
$\overline{P}_{out}$	1.125
$\bar{h}^*$	20.0

Figs. 6–8 display plots of the dimensionless pressure $\overline{P}$, temperature $\overline{T}$, and moisture (1-S) profiles across the sphere radius at various charging times, respectively. Fig. 6 shows a steep pressure peak close to the sphere surface. During the charging phase, this peak in pressure rises and moves away from the sphere surface. The vapor that moves from the interface into the wet region quickly condenses as its pressure is reduced to the saturation pressure of the local temperatures. This condensation enhances the energy transport rate into the wet region. The total pressure buildup within the wet region is a consequence of: (a) the combined effects of vapor generation and transport into the wet region; and (b) air "entrapment" with simultaneous volumetric and thermal compression. Fig. 7 shows the surface temperature of the sphere rising abruptly and continuing to increase due to the constant elevated fissure temperature. Initially, the temperature gradient at the sphere surface is very steep,

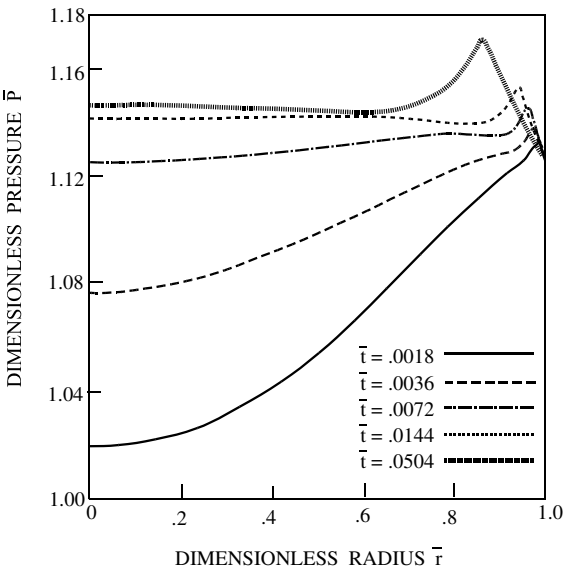

Fig. 6. Dimensionless pressure distributions within the sphere at various times.

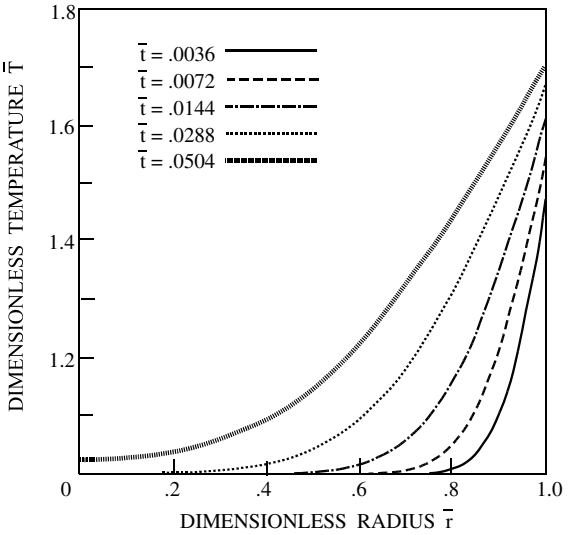

Fig. 7. Dimensionless temperature distributions within the sphere at various times.

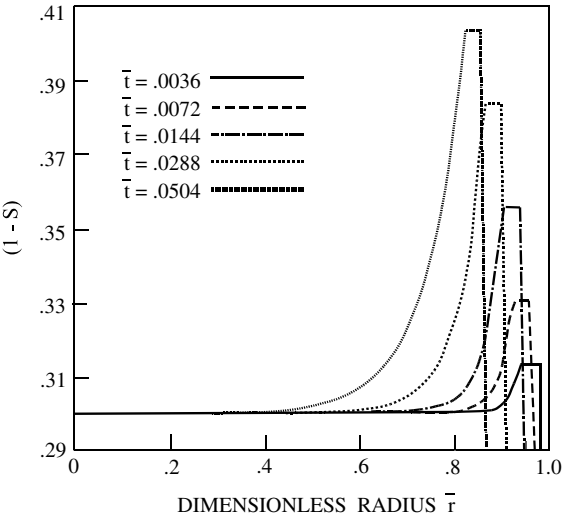

Fig. 8. Distribution of the pore liquid saturation (pore volume fraction occupied by liquid) within the sphere at various times.

but decreases as the sphere heats up. Fig. 8 displays the accumulation of moisture adjacent to the interface, which occurs due to pressure driven moisture convection towards the wet zone as well as vapor condensation, as required by local thermodynamic equilibrium considerations. The build-up of moisture moves inwards concurrently with the migration of the interface and is seen to rise steadily over time. Compared to the planar case, moisture accumulation is steeper due to the decreasing interface surface area with drying progression.

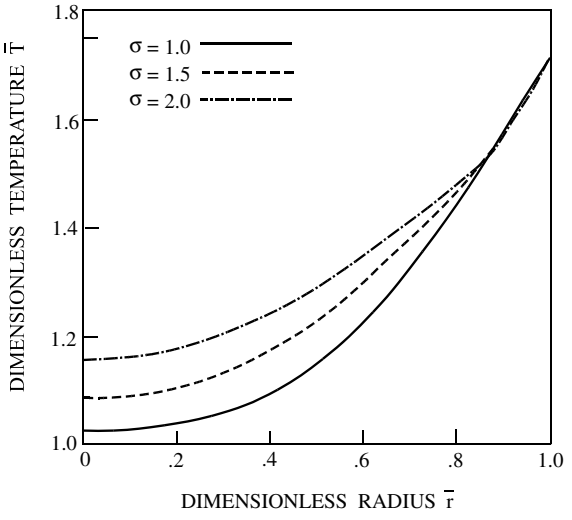

Fig. 9. Dependence of the dimensionless temperature distribution on the ratio of the wet to dry zones thermal conductivity, σ, at a dimensionless time of 0.0504.

Fig. 9 shows the influence of the ratio of wet over dry thermal conductivities σ on the temperature profile at a dimensionless time $\bar{t} = 0.0504$. The interface location manifests itself in an abrupt change in the temperature gradient around $\bar{r} = 0.85$ for σ above unity. For $\sigma = 1$, however, the curve is smooth and the interface position is not apparent (although it can easily be detected in the pressure curve—Fig. 6). Close examination of the interface region for σ not equal to unity and comparison with the interface location in Fig. 6 shows that σ does not appreciably affect the rate of the dry/wet interface advancement. The greater the value of σ, the higher the wet zone temperature and the steeper the dry zone temperature gradient.

Fig. 10 displays the influence of the dimensionless fissure temperature on the rate of vapor release from the sphere surface over time. The greater the fissure temperature, the greater the rate of vapor release. At high fissure temperatures, the vapor release rises steeply during the initial heating period. After quickly reaching a peak, the release slowly decreases as the evaporation front (wet/dry interface) advances towards the sphere center. Each curve levels as the rate of movement of the interface slows due to accumulation of moisture ahead of the front (as witnessed in Fig. 8). Effectively, moisture accumulation enhances the thermal inertia by increasing the apparent heat capacity at the front. Interface movement is especially slow for a low fissure temperature, where the surface heat flux is too weak to supply the large latent heat necessary for fast moisture evaporation.

To simulate the operation of a compressed air energy storage unit, a periodic charge/discharge cycle is con-

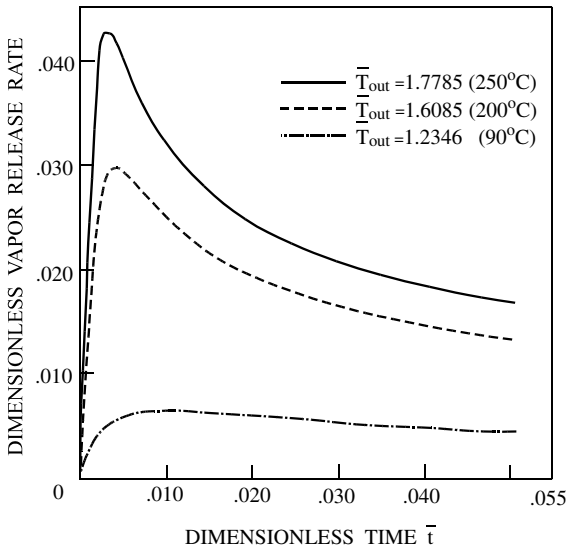

Fig. 10. Dimensionless flux of vapor released from the heated sphere surface for different surface temperatures.

sidered. In the first 48 h the fissure pressure is gradually raised to 40 atm. It is then allowed to fluctuate in 24 h cycles, where the pressure varies in a sinusoidal fashion with an amplitude of 5 atm (simulating charging/discharging). During the cyclical charging phase the fissure temperature is held constant at 250 °C, which slowly drops linearly during discharge to levels ranging from 150 to 235 °C. Fig. 11 shows the cumulative vapor loss from a sphere of 1 m radius. The characteristic thermal

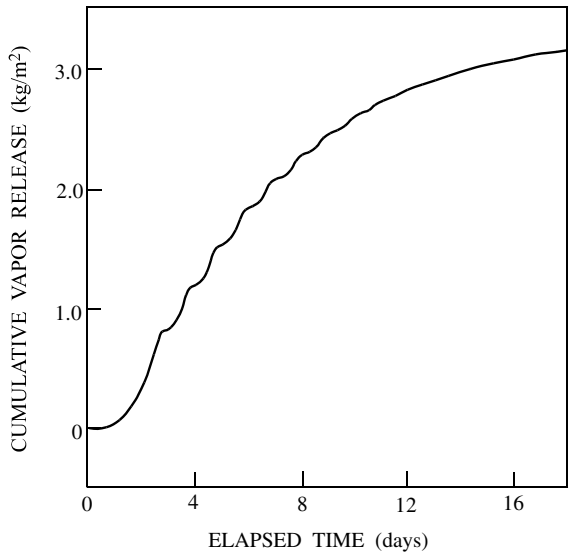

Fig. 11. Time history of the cumulative discharged mass of vapor per unit surface area for a periodic heating of the sphere surface.

Table 3
Input material properties for the periodic charging analysis

ρ_0	2100.0 kg/m^3
C_0	800.0 J/(kg °C)
K_d	1.8 W/(m °C)
K_w	1.9 W/(m °C)
ε	0.05
k/μ_g	5.0×10^{-12} m^2/(Pa s)
β	5.0×10^{-3}
D	1.2×10^{-7} m^2/s
T_s	21.0 °C
P_s	1.0×10^5 Pa
S_s	0.8

properties can be found in Table 3. During the initial 24 hours an isothermal compression is maintained and, consequently, there is no vapor loss. Once the fissure temperature rises, however, the charging/discharging cycle begins and the vapor loss rises quickly. The fluctuations (wavy behavior) in the curve are caused by the cyclical nature of the sphere boundary conditions, i.e., of the fissure temperature and pressure. After a period of about 12 days, vapor loss begins to level off as the sphere drying rate slows due to the substantially reduced moisture content. After 17 days and 21 hours the total water loss from the sphere is 39.71 kg, from an initial water content of 41.89 kg.

5. Conclusions

A detailed model of heat and mass transport mechanisms of hot compressed air impregnation for underground energy storage has been developed for homogeneous porous spherical rocks. The wet/dry interface can be followed as drying proceeds and vapor is removed from the sphere. Simulations reveal the sensitivity of the transport mechanisms to various dimensionless parameters of the operating conditions. Interestingly, the enhancement of thermal inertia due to moisture presence within the pore space appears to be a dominant factor in the drying process. Accumulation of moisture adjacent to the wet/dry interface is shown to have a strong effect in slowing the evaporation front movement.

This work is the first stage of the development of a comprehensive design and analysis tool for compressed air energy storage systems. Large underground storage aquifers can be subdivided into distinct homogeneous blocks applying a statistical distribution of sphere size and fracture lengths; the model presented would provide detailed thermal/mass transport response of individual blocks to compressed air charging and discharging operating modes. The results from the single sphere model could be integrated into a larger model as a correlational sub-model. Alternatively, a micro–macro

modeling approach for transport in porous media, as in [20], could be employed.

References

[1] Elliot, Electric energy storage hinges on three leading technologies, Power 139 (1995) 42–45.

[2] Cohn, Power plant cycles featuring air humidification, EPRI J. 18 (1993) 43–47.

[3] Y.S.H. Najjar, M.S. Zaamout, Performance analysis of compressed air energy storage (CAES) plant for dry regions, Energy Conver. Manage. 39 (15) (1998) 1503–1511.

[4] D.R. Hounslow, W. Grindley, R.H. Loughlin, The development of a combustion system for a 110 MW CAES plant, J. Eng. Gas Turbines Power 120 (4) (1998) 875–883.

[5] C.H. Lee, I. Farmer, Fluid flow in discontinuous rocks, first ed., Chapman and Hall, London, 1993.

[6] M. Kaviany, Principles of Heat Transfer in Porous Media, Springer-Verlag, New York, 1995, Chapter 12.

[7] L.D. Stewart, K.S. Udell, The effect of gravity and multiphase flow on the stability of condensation fronts in porous media, in: Multiphase Transport in Porous Media-1989, ASME HTD-Vol. 127 (FED-Vol. 82), 1989, pp. 29–37.

[8] K. Hanamura, M. Kaviany, Propagation of condensation front in steam injection into porous dry media, Int. J. Heat Mass Transfer 38 (1995) 1377–1386.

[9] J. Hager, S. Whitaker, Vapor–liquid jump conditions within a porous media: results for mass and energy, Transport Porous Media 40 (1) (2000) 73–111.

[10] C.K. Ho, K.S. Udell, Mass transfer limited drying of porous media containing an immobile binary liquid mixture, Int. J. Heat Mass Transfer 38 (2) (1995) 339–350.

[11] S.K. Chou, M.N.A. Hawlader, K.J. Chua, Identification of the receding evaporation front in convective food drying, Drying Technol. 15 (5) (1997) 1353–1367.

[12] A. Dayan, E.L. Gluekler, Heat and mass transfer within an intensely heated concrete slab, Int. J. Heat Mass Transfer 25 (10) (1982) 1461–1467.

[13] C. Yu, C. Loureiro, J.-J. Cheng, L.G. Jones, Y.Y. Wang, Y.P. Chia, E. Faillace, Data collection handbook to support modeling impacts of radioactive material in soil, internal report, Argonne National Laboratory, Environmental Assessment and Information Sciences Division, April 1993. Available from <www.ead.anl.gov/resrad/documents/data_collection.pdf>.

[14] A. Dayan, Self-similar temperature, pressure and moisture distributions within an intensely heated porous space, Int. J. Heat Mass Transfer 25 (10) (1982) 1469–1476.

[15] H. Saito, N. Seki, Mass transfer and pressure rise in moist porous material subjected to sudden heating, J. Heat Transfer 99 (1) (1977) 105–112.

[16] G.D. Smith, Numerical solution of partial differential equations—finite difference ethods, second ed., John Wiley, New York, 1973.

[17] J.D. McCormack, A.K. Postma, J.A. Schur, Water evolution from heated concrete, Hanford Engineering Development Laboratory, HEDL Report No. TME 78-87/UC-79h, 1979.

[18] J. Flesh, Heat and mass transfer in a porous spherical rock with phase change, MS Thesis, Tel-Aviv University, 1989.

[19] T.Z. Harmathy, L.W. Allen, Thermal properties of selected masonry unit concretes, J. Am. Concr. Inst. 70 (1973) 132–142.

[20] A. Martin, C. Saltiel, W. Shyy, Frictional losses and convective heat transfer in sparse, periodic cylinder arrays in cross flow, Int. J. Heat Mass Transfer 41 (15) (1998) 2383–2397.